PNAS RESEARCH ARTICLE | BIOCHEMISTRY CHEMISTRY OPEN ACCESS

Biochemical and structural characterization of a sphingomonad diarylpropane lyase for cofactorless deformylation

Eugene Kuatsjah[a], Michael Zahn[b], Xiangyang Chen[c], Ryo Kato[d], Daniel J. Hinchen[b], Mikhail O. Konev[a], Rui Katahira[a], Christian Orr[e], Armin Wagner[e], Yike Zou[c], Stefan J. Haugen[a], Kelsey J. Ramirez[a], Joshua K. Michener[f], Andrew R. Pickford[b], Naofumi Kamimura[d], Eiji Masai[d,1], K. N. Houk[c,1], John E. McGeehan[b,1,2], and Gregg T. Beckham[a,1]

Edited by Uwe T. Bornscheuer, Universitat Greifswald, Greifswald, Germany; received August 15, 2022; accepted November 27, 2022 by Editorial Board Member Stephen J. Benkovic

Lignin valorization is being intensely pursued via tandem catalytic depolymerization and biological funneling to produce single products. In many lignin depolymerization processes, aromatic dimers and oligomers linked by carbon–carbon bonds remain intact, necessitating the development of enzymes capable of cleaving these compounds to monomers. Recently, the catabolism of *erythro*-1,2-diguaiacylpropane-1,3-diol (*erythro*-DGPD), a ring-opened lignin-derived β-1 dimer, was reported in *Novosphingobium aromaticivorans*. The first enzyme in this pathway, LdpA (formerly LsdE), is a member of the nuclear transport factor 2 (NTF-2)-like structural superfamily that converts *erythro*-DGPD to lignostilbene through a heretofore unknown mechanism. In this study, we performed biochemical, structural, and mechanistic characterization of the *N. aromaticivorans* LdpA and another homolog identified in *Sphingobium* sp. SYK-6, for which activity was confirmed in vivo. For both enzymes, we first demonstrated that formaldehyde is the C_1 reaction product, and we further demonstrated that both enantiomers of *erythro*-DGPD were transformed simultaneously, suggesting that LdpA, while diastereomerically specific, lacks enantioselectivity. We also show that LdpA is subject to a severe competitive product inhibition by lignostilbene. Three-dimensional structures of LdpA were determined using X-ray crystallography, including substrate-bound complexes, revealing several residues that were shown to be catalytically essential. We used density functional theory to validate a proposed mechanism that proceeds via dehydroxylation and formation of a quinone methide intermediate that serves as an electron sink for the ensuing deformylation. Overall, this study expands the range of chemistry catalyzed by the NTF-2-like protein family to a prevalent lignin dimer through a cofactorless deformylation reaction.

lignin | aromatic catabolism | *Novosphingobium aromaticivorans* | *Sphingobium* sp. SYK-6 | NTF-2

Significance

The microbial conversion of lignin-derived aromatic compounds generated during the natural decay of plant matter is enabled by diverse aromatic-catabolic enzymes. To date, enzymes and metabolic pathways have been reported for the catabolism of many lignin-derived aromatic monomers and for some dimers resulting from lignin breakdown. Studies to this end are important both to gain a fundamental understanding of the biochemical mechanisms of recalcitrant carbon turnover in nature and to harness the potential of these enzymes for biotechnological applications, in this case for the valorization of lignin to chemicals. This study describes a diarylpropane lyase enzyme that catalyzes cofactorless C–C bond fission in a lignin-derived dimer via a unique tandem dehydroxylation and deformylation reaction.

Lignin valorization is integral to a viable lignocellulose-based bioeconomy (1). However, lignin remains a challenging substrate to convert into chemicals due to its recalcitrance and heterogeneity (2). To that end, bacterial biocatalysts enable convergent catabolism of mixtures of lignin-derived aromatic monomers into select value-added products, such as *cis*,*cis*-muconic acid, β-ketoadipic acid, and 2-pyrone-4,6-dicarboxylic acid through biological funneling processes (3–11). However, aromatic dimers and oligomers, often linked by carbon–carbon linkages, typically remain after many lignin deconstruction processes, prompting interest in the biological catabolism of aromatic dimers (5, 8). To date, *Sphingobium* sp. SYK-6 and *Novosphingobium aromaticivorans* DSM12444 (SYK-6 and *N. aromaticivorans*, hereafter) are among the best characterized strains capable of transforming various lignin-derived aromatic dimers linked by β-*O*-4, β-1, β-5, β-β, and 5-5 bonds (5, 12–15). While many of these dimers can be affected by peroxidases or laccases, it is becoming increasingly apparent that microbes have also evolved catabolic enzymes to enable their entry to the central metabolism without the sole reliance on diffusible radical species (11, 16).

The catabolism of the *erythro* diastereomer of the ring-opened β-1 dimer, 1,2-bis(4-hydroxy-3-methoxyphenyl)-1,3-propanediol (DGPD, also known as HMPPD), proceeds via the formation of lignostilbene (Scheme 1) and its subsequent oxidative cleavage to two molar equivalents of vanillin. This pathway was first described in *Sphingomonas paucimobilis* TMY1009 (TMY1009, hereafter) (17), but the gene sequence associated with the first step was not reported. Recently, the β-1 dimer catabolic pathway was rediscovered in *N. aromaticivorans* with a γ-formaldehyde lyase and the lignostilbene-α,β-dioxygenase (LSD, NOV2 in *N. aromaticivorans*) as the enzymes responsible for these transformations (18). The *threo*-DGPD diastereomer, conversely, is not converted by this enzyme pair and its catabolic pathway has not yet been reported to our knowledge. Here, we propose a renaming of the

The authors declare no competing interest.

This article is a PNAS Direct Submission. U.T.B. is a guest editor invited by the Editorial Board.

[1]To whom correspondence may be addressed. Email: emasai@vos.nagaokaut.ac.jp, houk@chem.ucla.edu, drjohnmcgeehan@gmail.com, or gregg.beckham@nrel.gov.

[2]Present address: World Plastics Association, Fontvieille, Monaco.

This article contains supporting information online at https://www.pnas.org/lookup/suppl/doi:10.1073/pnas.2212246120/-/DCSupplemental.

Published January 18, 2023.

γ-formaldehyde lyase to LdpA (lignin diarylpropane-associated catabolic enzyme), formerly known as LsdE, in the light of eight stilbene dioxygenases characterized in SYK-6, which are also referred to as Lsd enzymes (19, 20). The mechanism of the reaction catalyzed by LdpA was heretofore unknown, including the identity of the C_1 reaction product.

The *erythro*-DGPD γ-formaldehyde lyase, LdpA, belongs to the nuclear transport factor 2 (NTF-2)-like protein family that is exemplified by a twisted α + β barrel fold (21). Despite its name, some members of the NTF-2-like protein family are catalytic in nature, typically performing dehydration, dehydrochlorination, and more recently decarboxylation, as illustrated in Scheme 1. Characterized examples of NTF-2-like enzymes include: BaiE, a 3-oxo-Δ^4-chenodeoxycholyl-CoA dehydratase (22), scytalone dehydratase (SD) (23), LinA, a γ-hexachlorocyclohexane dehydrochlorinase (24), and gallate/protocatechuate decarboxylases (GDC) (25). Comparison between these systems reveals a common catalytic theme involving a conserved His-Asp dyad that functions as an acid–base catalyst and typically an electron-rich intermediate that is stabilized by an oxyanion hole, often formed by the phenolic group of tyrosine residues. Unlike the aforementioned examples, LdpA catalyzes a more complex reaction, namely a simultaneous methyl–hydroxyl elimination and dehydroxylation of a substrate with no obvious built-in electron sink.

In this study, we combined kinetic, structural, and computational analyses to gain insight into the molecular mechanism of LdpA from both *N. aromaticivorans* and *Sphingobium* sp. SYK-6. The latter was identified by sequence homology, and its essentiality for *erythro*-DGPD transformation was confirmed in vivo. Formaldehyde, and not formate, was identified as the C_1 reaction product, which mirrors the facile formaldehyde-eliminating lyase reaction of DGPD that occurs abiotically in alkaline conditions (26). LdpA was found to be subject to product inhibition by lignostilbene. The absolute diastereomeric specificity of LdpA for *erythro*-DGPD can be rationalized through an orchestrated hydrogen-bonding network between the substrate and key catalytic residues, revealed by the ligand-bound structures and consistent with a more thermodynamically favored binding pose of *erythro*-DGPD, determined by density functional (DFT) calculations. Together, a reaction mechanism for the dehydroxylation and deformylation of *erythro*-DGPD to lignostilbene was proposed that ultimately expands both the catalytic machinery of the NTF-2-like protein family and the repertoire of enzymes active on lignin-derived aromatic compounds for biological funneling.

Results

Identification of an LdpA Homolog in *Sphingobium* sp. SYK-6. Following the identification of a C_γ-formaldehyde lyase in *N. aromaticivorans* (*Na*LdpA, hereafter) and a prior description in TMY1009, we identified *ldpA* homologs in SYK-6 (5, 17, 18) via a homology search of the SYK-6 genome using *NaldpA* (SARO_2805) as the search query. We identified SLG_12650 (*SpldpA*, hereafter), with 81% amino acid sequence identity, as the reciprocal best hit (*SI Appendix,* Fig. S1). Like *Na*LdpA, *Sp*LdpA transforms *erythro*-DGPD to lignostilbene (*SI Appendix,* Figs S2 and S3*A*). Further, the cell extract of Δ*SpldpA* lost the ability to turn over *erythro*-

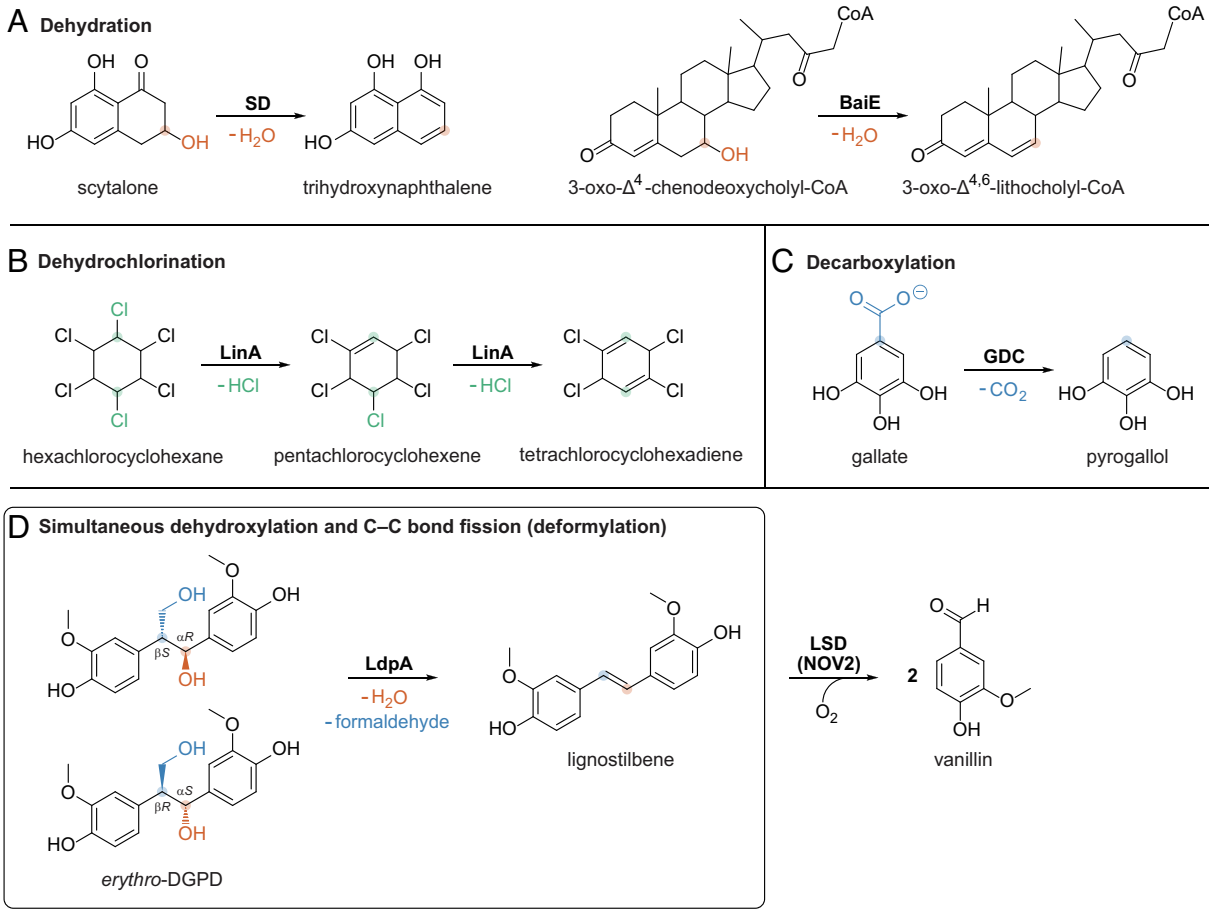

Scheme 1. Reactions catalyzed by NTF-2-like protein family scaffold.

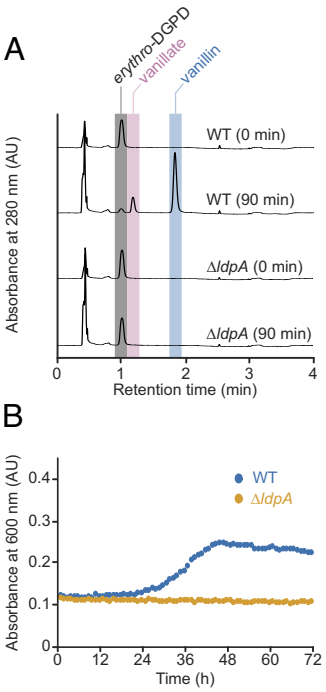

Fig. 1. In vivo transformation of *erythro*-DGPD by *Sp*LdpA in *Sphingobium* sp. SYK-6. (*A*) HPLC traces comparing the *erythro*-DGPD depletion when incubated with WT and Δ*SpldpA* SYK-6 cell extracts. Metabolites corresponding to *erythro*-DGPD [retention time (t_R) 1.1 min; *gray*], vanillate (t_R 1.3 min; *pink*), and vanillin (t_R 1.8 min; *blue*) are labeled. (*B*) Growth of WT (*blue*) and Δ*SpldpA* (*orange*) SYK-6 strains on *erythro*-DGPD as the sole carbon source.

DGPD (Fig. 1*A*). Similarly, the deletion of *SpldpA* abrogated the ability of the strain to grow on *erythro*-DGPD as a sole carbon source, indicating that there is no substitute for LdpA for *erythro*-DGPD utilization (Fig. 1*B*). Notably, both *N. aromaticivorans* and SYK-6 encode several NTF-2-like homologs with ≤40% protein sequence identity to LdpA (*SI Appendix,* Fig. S1); however, these homologs do not appear to affect either diastereomeric forms of DGPD (*SI Appendix,* Fig. S2 *A* and *B*).

LdpA Deformylates DGPD with a Strict Diastereomeric Selectivity. To investigate the catalytic properties of these enzymes, *Na*LdpA and *Sp*LdpA were heterologously produced in *Escherichia coli* and purified to homogeneity. Purified LdpA appears colorless and lacks a spectroscopic signature in the visible range, reflecting the cofactorless nature of the enzyme. Like prior observations, both LdpA enzymes are specific to *erythro*-DGPD and not reactive toward *threo*-DGPD (*SI Appendix,* Figs. S2 and S3) (18). Additionally, we also investigated whether LdpA can transform other substrate analogs including 1-(4-hydroxy-3-methoxyphenyl)-1,3-propanediol (GPD), guaiacylglycerol-β-guaiacyl ether (GGE) – a β-*O*-4 dimer, and dehydrodiconiferyl alcohol (DCA) – a furan-type β-5 dimer (*SI Appendix*, Scheme S1). GPD was tested to evaluate the contribution of the C_β-guaiacyl group for catalysis and substrate binding. GGE is isomeric to DGPD and differs only in how the C_β-guaiacyl group is connected to the central propanediol moiety. DCA and DGPD share a stilbene-type downstream intermediate. None of the substrate analogs, however, were transformed by either LdpA.

The LdpA-catalyzed reaction with *erythro*-DGPD does not consume oxygen, suggesting that this process is nonoxidative in nature. Additionally, the pH-dependent activity profiles reveal that both LdpA enzymes are most active near pH 7.0 with *Sp*LdpA relatively more active at acidic pH, while the opposite is true for *Na*LdpA (*SI Appendix*, Fig. S4 and Table S1). Thus, all subsequent enzyme assays were performed in air-saturated MOPS [ionic strength (I) = 0.1 M, pH 7.0].

Formaldehyde, and not formate, was identified as the C_1 reaction product as determined using formaldehyde- and formate-specific dehydrogenases (*SI Appendix,* Fig. S5), and 1.3 ± 0.1 mol formaldehyde for every mol of O_2 was consumed in an *Na*LdpA·NOV2-coupled reaction. This reaction stoichiometry is consistent with the purported activity of *Na*LdpA and NOV2 with 1.0 ± 0.1 mol O_2 consumed, with 2.3 ± 0.1 mol vanillin produced per mol *erythro*-DGPD supplied.

DGPD contains two stereocenters along its propanediol moiety (C_α and C_β) and therefore, each diastereomer may exist as four distinct enantiomeric forms: (α*R*, β*R*) and (α*S*, β*S*) for *threo*-DGPD and (α*R*, β*S*) and (α*S*, β*R*) for *erythro*-DGPD. The DGPD preparations used in our studies were not synthesized using chiral auxiliary or precursors compounds, and thus are racemic for each diastereomeric form. While LdpA and NOV2 have been shown to completely turn over racemic *erythro*-DGPD in vivo (18), we sought to determine whether LdpA prefers one enantiomer over another by monitoring their depletion using chiral chromatography. While we were unable to assign the absolute stereochemistry of these peaks, the amount of *erythro*-DGPD consumed in a *Na*LdpA·NOV2 coupled reaction was commensurate with the amount of oxygen consumed, and both enantiomers were depleted simultaneously (Fig. 2). Together, the data show that *Na*LdpA lacks enantioselectivity. We subsequently determined the steady-state kinetic parameters of *Na*LdpA using oxygraphy to couple the production of lignostilbene to the activity of NOV2 due to product inhibition kinetics (*vide infra*). Both LdpA efficiently catalyze the elimination of formaldehyde from racemic *erythro*-DGPD with comparable kinetic parameters (Table 1 and *SI Appendix,* Fig. S6).

LdpA Is Subject to Product Inhibition. The activity of LdpA rapidly diminished to a negligible rate prior to the complete depletion of *erythro*-DGPD, which is indicative of some form(s) of inhibition (*SI Appendix,* Fig. S7). The initial velocity of the LdpA-catalyzed reaction was not affected in the presence of *threo*-DGPD, vanillin, or formaldehyde; however, the rate decreased by ~90% in the presence of 20 μM lignostilbene (*SI Appendix,* Fig. S8 and Table S5), consistent with product inhibition of LdpA by lignostilbene. Additional evidence for product inhibition was obtained from isothermal titration calorimetry (ITC). An endothermic reaction was observed when *erythro*-DGPD was injected into a solution of LdpA (ΔH_{app} of 9.70 kcal/mol at 25 °C; *SI Appendix,* Fig. S9), demonstrating that the conversion is entropically driven. In a dual-injection experiment, in which substrate is twice injected to a concentration of approximately 70 μM, the second injection of substrate elicits a much slower uptake of heat, indicating that the reaction is indeed susceptible to product inhibition.

Subsequently, kinetic assays using varying concentrations of lignostilbene and *erythro*-DGPD were performed to investigate the nature of this inhibition. The kinetic parameters obtained using the spectrophotometric method are consistent with prior oxygraphy measurements. Lignostilbene functions as a potent competitive inhibitor of LdpA (Fig. 3 and Table 1). As these K_{ic} values are approximately ~50-fold lower than the K_M for *erythro*-DGPD, a significant product inhibition is expected when LdpA functions in isolation. Furthermore, if K_{ic} values are used to approximate the K_d and the lignostilbene association rate (k_{on}) is diffusion controlled, the estimated lignostilbene dissociation rate (k_{off}) is only an order magnitude higher than the observed k_{cat}, suggesting that the product release may be rate limiting.

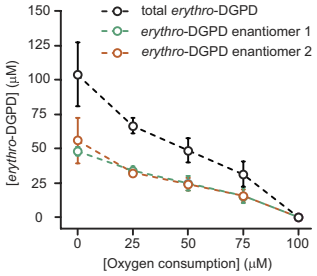

Fig. 2. Simultaneous consumption of *erythro*-DGPD enantiomers by LdpA. The depletion of *erythro*-DGPD enantiomers as followed by chiral chromatography. The reaction was sampled following 0, 25, 50, 75, and 100 μM oxygen consumption in a mixture containing 100 μM racemic *erythro*-DGPD, *Na*LdpA, and NOV2. The *green* and *orange* traces represent the individual enantiomers, and the *black* trace represents the total *erythro*-DGPD. The measurements were an average of three replicates and the error bars are the SD. The numerical data are provided in the *SI Appendix,* Table S2.

The LdpA Trimer Employs a Dual Motif Arrangement That Confers Exquisite Active Site Coordination of the *erythro*-DGPD Substrate. To gain further insights into the catalytic machinery of LdpA, we solved several X-ray crystal structures, including ligand-bound complexes (Fig. 4 and *SI Appendix,* Table S6). We obtained well-diffracting crystals with resveratrol, a product analog (1.39 Å resolution, *SI Appendix,* Fig. S10). The *Na*LdpA structure was solved via single-wavelength anomalous diffraction of sulfur atom (S-SAD) phasing (27). In parallel, we obtained diffraction data of *Sp*LdpA in complex with *erythro*- and *threo*-DGPD at a resolution of 1.68 and 1.71 Å, respectively, and solved the structures by molecular replacement using the resveratrol-bound *Na*LdpA structure (81% sequence identity).

*Sp*LdpA and *Na*LdpA belong to the NTF2-like structural superfamily and form a cone-shaped barrel consisting of a twisted β-sheet and three α-helices (Fig. 4*A* and *SI Appendix,* Fig. S11). The overall fold of both structures is almost identical with a rmsd of 0.4 Å. The closest structural homolog according to the DALI server (28) is γ-hexachlorocyclohexane dehydrochlorinase, LinA (PDB 3A76) with an rmsd of 1.8 Å (139 aligned residues), despite only sharing 18% primary sequence identity (24). LdpA forms a homotrimer that is stabilized by the extended C-terminal arm of one monomer making extensive contacts with an adjacent monomer (Fig. 4 *B* and *C*).

A trimeric assembly for LdpA was also confirmed in solution as determined by tandem size-exclusion chromatography and small-angle X-ray scattering (SEC-SAXS) (*SI Appendix,* Fig. S13). The thermostability of the LdpA trimer was assessed by differential scanning calorimetry (DSC). A single melting transition for the enzyme was observed at 49.9 ± 0.4 °C, which we interpret as the simultaneous breakdown of both the trimeric assembly with concomitant denaturation of the component monomer domains (*SI Appendix,* Fig. S14). This stability profile (for a mesophilic enzyme) suggests that the trimeric biological assembly is a stable entity at the temperature used for functional assays (25 °C).

Cocrystallization of wild-type (WT) *Na*LdpA with DGPD was unsuccessful, but we obtained a complex structure with the catalytically inactive mutant enzyme His97Gln (*vide infra*) with (α*S*, β*R*)-*erythro*-DGPD (*SI Appendix,* Fig. S15). The substrate-binding mode is equivalent in the *Na*LdpA-His97Gln variant and WT *Sp*LdpA (*SI Appendix,* Fig. S15), suggesting that this crystal structure is representative of the productive substrate-binding mode. The electron density of *Sp*LdpA suggests binding of both enantiomers, which were each built with half occupancy (Fig. 4*E* and *SI Appendix,* Fig. S12).

The central propanediol component of DGPD resides between two strongly coordinated protein motifs in *Sp*LdpA (Fig. 4 *D*–*F*). The first (Motif I) is the His93-Asp36 dyad, which coordinates the C_γ-hydroxyl group of the substrate. This is conserved in other NTF-2-like enzymes and functions as the key acid–base catalyst (22, 29). The second (Motif II) is a triad formed by residues Glu139-Tyr161-Gln166 triad, which coordinates the C_α-hydroxyl group of the substrate. This is an exclusive motif to LdpA and appears to contribute to the substrate-binding preference (along the perpendicular to the propanediol axis), where the specific interactions of the C_α- and C_γ-hydroxyl group confer orientational preference.

In contrast to the *erythro*-DGPD propanediol binding interactions, the bound *threo*-DGPD enantiomers [(α*S*, β*S*) and (α*R*, β*R*)] exhibit either extended distances or generally less favorable interactions between the hydrogen-bond donors and acceptors (Fig. 4 *F* and *G* and *SI Appendix,* Fig. S12 *C* and *D*), although the overall interactions between DGPD and *Sp*LdpA remain similar. The hydroxyl and methoxy groups of the α-guaiacyl DGPD residue form hydrogen bonds with multiple tyrosine side chains (Tyr31, Tyr70, and Tyr143) (Fig. 4 *D*–*F* and *SI Appendix,* Fig. S12), and Tyr161 forms a π-stacking interaction to the α-guaiacyl aromatic ring. The β-guaiacyl phenolic group forms hydrogen bonds to Arg77 and His179. Notably, these interactions were not observed in the *Na*LdpA structure, due to the loop bearing these two residues being less ordered and the arginine residue substituted by a leucine. Overall, the β-guaiacyl group is not as extensively coordinated as the α-guaiacyl residue. This may reflect the flexibility of LdpA to accept β-1 dimers derived from *p*-coumaryl (H) or syringyl (S)-type precursors and may be useful in future engineering studies (18).

Confirmation of Key Active Site Residues by Mutagenesis. Following the determination of substrate-bound structures and the homology to other NTF-2-like structures, seven *Na*LdpA active site residues (Tyr35, Asp40, Tyr74, His97, Glu143, Tyr147, and His183) were selected for mutational analysis based on the ligand-bound crystal structures. Each of the variants was produced at equivalent yields to their WT counterpart, allowing us to assess their comparative contributions to catalysis (Fig. 5). As predicted from the structural analysis, the Motif I dyad formed by His97

Table 1. Kinetic parameters of LdpA

	Oxygraph			Spectrophotometer			
Enzyme	k_{cat} s^{-1}	K_M μM	k_{cat}/K_M $\times 10^5\ s^{-1}.M^{-1}$	k_{cat} s^{-1}	K_M μM	k_{cat}/K_M $\times 10^5\ s^{-1}.M^{-1}$	$K_{ic\ lignostilbene}$ μM
*Na*LdpA	2.6 ± 0.2	11.9 ± 0.6	2.2 ± 0.2	2.36 ± 0.06	15 ± 1	1.6 ± 0.1	0.33 ± 0.03
*Sp*LdpA	2.1 ± 0.2	13.1 ± 0.6	1.6 ± 0.2	2.11 ± 0.06	16 ± 1	1.3 ± 0.1	0.26 ± 0.02

Experiments were performed using air-saturated MOPS (I = 0.1 M), pH 7.0, 25 °C. The oxygraph-based assays, coupled with the activity of NOV2, followed the consumption of O_2 and the spectrophotometer-based assays, independent of NOV2, followed the production of lignostilbene. The error represents SEs from fitting the Michaelis–Menten equation to the data. The numerical data used to determine these kinetic parameters are provided in the *SI Appendix,* Tables S3 and S4.

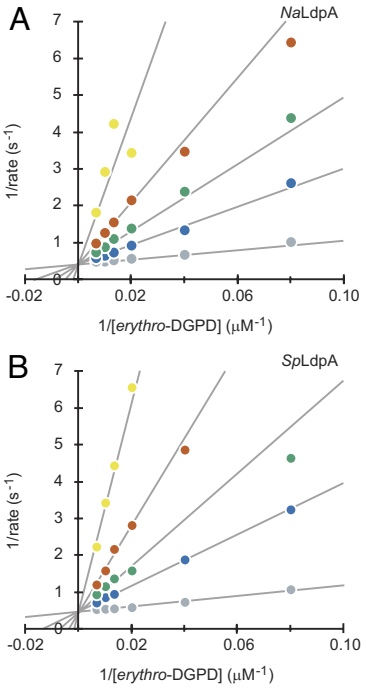

Fig. 3. Lineweaver–Burk plot of the inhibition of LdpA-catalyzed *erythro*-DGPD deformylation by lignostilbene. Experiments for *Na*LdpA (*A*) and *Sp*LdpA (*B*) were performed in MOPS (*I* = 0.1 M, pH 7.0), 25 °C, and 0 (*gray*), 1 (*blue*), 2 (*green*), 4 (*red*), and 10 (*yellow*) μM lignostilbene. The lines represent a best fit of an equation describing competitive inhibition to the data, *Na*LdpA, k_{cat} = 2.36 ± 0.06 s^{-1}; K_M = 15 ± 1 μM; K_{ic} = 0.33 ± 0.03 μM, and *Sp*LdpA, k_{cat} = 2.11 ± 0.06 s^{-1}; K_M = 16 ± 1 μM; K_{ic} = 0.26 ± 0.02 μM. The numerical data used to determine these kinetic parameters are provided in the *SI Appendix*, Table S4.

and Asp40 is functionally important and substitutions of His97 to either glutamine or alanine and Asp40 to alanine abrogated the enzymatic activity. A more conservative substitution of Asp40 to asparagine was tolerated, but still lowered the catalytic activity by approximately fivefold. In terms of Motif II, removal of the Glu143 carboxylate group by substitution to glutamine and alanine rendered the enzyme completely inactive. Mutations of neighboring tyrosine residues (Tyr35 and Tyr147) that interact with the phenolic hydroxyl group of the substrate resulted in inactive enzymes, while the substitution of a tyrosine (Tyr74) that interacts with the methoxy group only lowered the enzyme activity by 30%. Finally, His183, whose equivalent was found to interact with the phenolic hydroxyl group of the C_β-guaiacyl group in the substrate of *Sp*LdpA, was modified to glutamine and alanine, both of which lowered the catalytic activity by approximately fivefold. Overall, these results are consistent with His97 and Glu143 as putative acid–base residues and Tyr35 and Tyr147 as the putative oxyanion hole.

LdpA Catalyzes the Transformation of *erythro*-DGPD Through a Quinone-Methide Intermediate. Based on the precedent of NTF-2-like dehydratase (22, 29) and the data presented in this study, we propose a mechanism for LdpA that proceeds via a dehydroxylation step to form a quinone-methide intermediate, followed by a deformylation step. This mechanism is related to the facile elimination of formaldehyde from a DGPD-derived quinone methide under abiotic alkaline conditions (26). The proposed mechanism is summarized in Fig. 6*A*. The reaction is initiated by the deprotonation of the C_α phenol group by Glu143 (*Na*LdpA numbering) as *erythro*-DGPD enters the LdpA active site. Considering its considerable distance, Glu143 is unlikely to abstract the C_α phenolic proton of *erythro*-DGPD directly, and this process may proceed through a proton-relay process as aided by Tyr165 and Tyr147, perhaps in a concerted manner. The substrate C_α phenolate anion is stabilized by hydrogen bonding by Tyr35 and Tyr147, which together serve as an oxyanion hole. Electron delocalization from the phenolate ion leads to the dehydroxylation at the C_α site, catalyzed by Glu143 acting as an acid catalyst to protonate the leaving hydroxyl group. The resulting quinone methide intermediate provides the requisite electron sink necessary for C–C fission. His97 abstracts the C_γ-hydroxyl group, leading to the fragmentation of the C_β–C_γ bond (thus liberating formaldehyde), the formation of the *trans* C_α–C_β bond, and the regeneration of the phenolate ion. Ultimately, lignostilbene leaves the active site and is reprotonated by His97, thereby returning the redox state of the enzyme into its resting state.

Free Energy Level Trajectories Associated with *erythro*-DGPD Complexes Are More Stable Than Their *threo* Counterparts. The feasibility of the proposed mechanism and the rationale for the enantioselectivity were established by DFT performed at the level of B3LYP-D3(BJ)/6-31G(d,p), SCRF = (CPCM, Solvent = water) (Fig. 6*A*, *SI Appendix*, Figs. S16–S19 and Tables S8 and S9). To mimic the enzyme environment, several simplified cluster models derived from the crystal structures were used to support the model used for the calculations (*SI Appendix*, Fig. S18). The different reaction coordinates are denoted as IN and TS for intermediates and transition states, respectively, which are followed by a numerical notation, Arabic for the intermediates and Roman for the transition states, to denote their order of appearance.

The calculated free energy profiles for various stereoisomeric substrates are summarized in Fig. 6*B*. First, we calculated the energy level for the enzyme–substrate complex for (α*R*, β*S*)-*erythro*-DGPD and use (α*R*, β*S*)-IN0 as the reference point for the subsequent energy states. For (α*R*, β*S*)-*erythro*-DGPD, the deprotonation of the C_α phenol group forms a metastable intermediate (α*R*, β*S*)-*erythro*-IN1. The dehydroxylation at the C_α site through (α*R*, β*S*)-*erythro*-TSI is more facile, with a free energy of 10.6 kcal/mol and forming a 1.6 kcal/mol less stable quinone methide intermediate. The release of the formaldehyde through (α*R*, β*S*)-*erythro*-TSII is 14.5 kcal/mol. The energetics for another *erythro*-enantiomer and the *threo*-diastereomers were also analyzed. As shown in Fig. 6*B*, the route for (α*R*, β*S*)-*erythro*-DGPD is comparable to that of its enantiomer, passing through (α*S*, β*R*)-*erythro*-TSI with a free energy barrier of 11.0 kcal/mol and (α*S*, β*R*)-*erythro*-TSII with a free energy barrier of 14.1 kcal/mol; this is consistent with the observation where the two *erythro* enantiomers are consumed simultaneously. The antiperiplanar alignment of the hydroxymethyl group with the benzylic hydroxy group facilitates the antielimination in the *erythro* configuration; whereas the gauche alignment of those two groups in the *threo* configuration requires more geometric changes to generate the olefin product, thereby more distortion is involved in the transition state. As shown in Fig. 6*B*, the energy profile of *threo*-DGPD pathways is always higher than that of the *erythro*-DGPD pathway along the reaction coordinate with an energy barrier of 33.1 kcal/mol and 42.9 kcal/mol, respectively, and agrees with the observation that *threo*-DGPD is not transformed by LdpA. Similarly, the free energy for IN0 of *threo*-DGPD is at least 8.3 kcal/mol higher than that of *erythro*-DGPD or lignostilbene, indicating that this diastereomer would not act as an inhibitor (*SI Appendix*, Fig. S8). By contrast, the energy of IN3 (lignostilbene) is equivalent to that of IN0 (*erythro*-DGPD), which corroborates the aforementioned product inhibition (Fig. 3). Further, a theoretical study with a 180° flipped binding orientation (α*R*, β*S*)-*erythro*-DGPD, where (α*R*, β*S*)-*erythro*-TSI binding mode is flipped such that the role of catalytic histidine and glutamate is swapped, was investigated. This pathway (Path

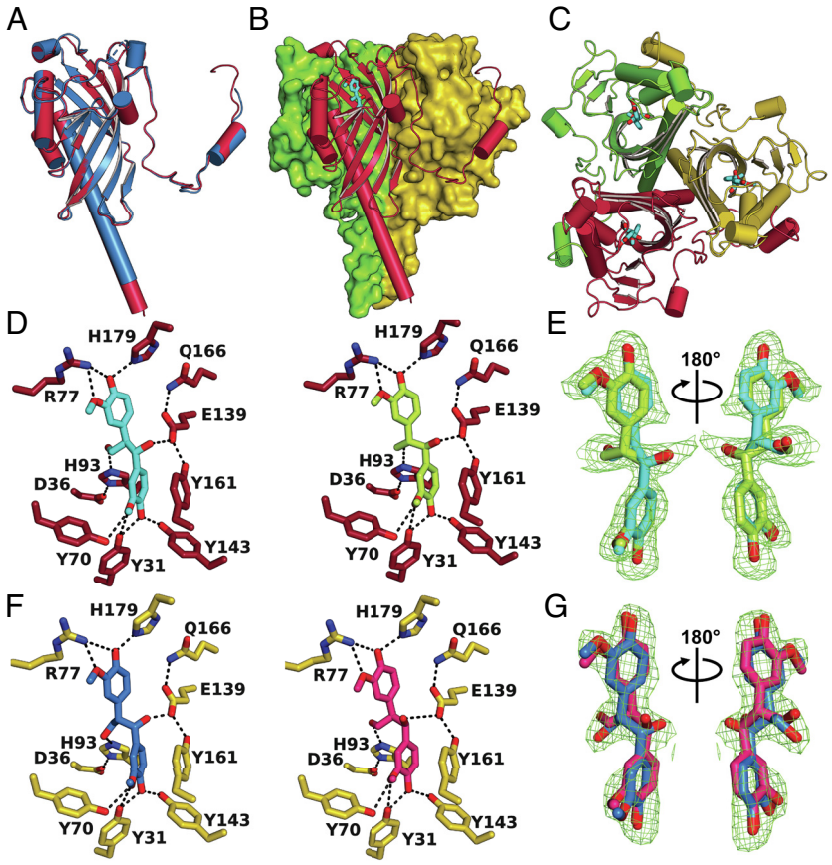

Fig. 4. Structural architecture of LdpA and substrate interactions. (*A*) Superposition of *Sp*LdpA (*magenta*) with *Na*LdpA (*teal*). (*B*) Side view of the *Sp*LdpA trimer. Two protein chains are shown as surfaces (*yellow* and *green*) and one protein chain is shown in cartoon mode (*red*) with bound substrate *erythro*-DGPD (*light blue*). (*C*) *Top* view of the *Sp*LdpA trimer. (*D*) Pseudo-stereoscopic view of the interaction of *Sp*LdpA with the *erythro*-DGPD enantiomers (α*S,* β*R*) (*Left*) and (α*R,* β*S*) (*Right*). When viewed in stereo, alternating eye switching results in an optimal impression of the binding modes of the two diastereomer substrates. (*E*) Omit electron density map for the (α*S,* β*R*)- and (α*R,* β*S*)-*erythro*-DGPD enantiomers bound to *Sp*LdpA at 2.5 σ level. (*F*) Pseudo-stereoscopic view of the interaction of *Sp*LdpA with the *threo*-DGPD enantiomers (α*S,* β*S*) (*Left*) and (α*R,* β*R*) (*Right*). (*G*) Omit electron density map for the (α*S,* β*S*)- and (α*R,* β*R*)-*threo*-DGPD enantiomers bound to *Sp*LdpA at 2.5 σ level. A version of *D* and *F* with annotated polar distances is provided in the *SI Appendix,* Fig. S12.

B), however, has a much higher barrier of 25.4 kcal/mol from (α*R,* β*S*)-*erythro*-IN1′ to (α*R,* β*S*)-*erythro*-TSII′ as shown in *SI Appendix,* Fig. S20. Other possible mechanisms, including one that invokes the formation of a carbocation upon water release, were also evaluated. In this pathway (carbocation pathway), the catalytic glutamate is protonated without the concomitant deprotonation of the C_α phenolic proton of *erythro*-DGPD; nonetheless, this process is quite unfavorable even with acetic acid as the proton donor with a free energy barrier of 11.7 kcal/mol, *SI Appendix,* Fig. S21. Furthermore, the free energy barrier in the cationic mechanism goes as high as 29.3 kcal/mol (*SI Appendix,* Fig. S22) which is significantly higher than the free energy barrier of 14.5 kcal/mol in the proposed pathway (Fig. 6*B*). Together, these results are in line with the reported biochemical observations and offer mechanistic insights into the enantioselectivity of LdpA.

Discussion.

The reaction catalyzed by LdpA expands the range of chemistries of the enzymes belonging to the NTF-2 protein family. Despite catalyzing a more complex reaction, LdpA retains key features from the NTF-2 dehydratase and decarboxylase, including the use of the His-Asp dyad as an acid–base catalyst and tyrosines that function as an oxyanion hole. Typical substrates for enzymes from the NTF-2-like protein family including dehydratases contain an electron sink in the form of a β-keto group or equivalent structures as well as additional conjugated system (22, 23) or a good leaving group such as a β-chloro group in the case of dehydrochlorinase (29). Such a feature is missing in DGPD, and thus necessitates the recruitment of an additional Motif II, an Glu-Tyr-Gln triad, to facilitate the dehydroxylation step and the formation of the quinone methide electron sink. It is conceivable that the recently discovered gallate/protocatechuate decarboxylation may also employ the same form of intermediate (25). Notably, the free energies of the two transition states in the LdpA-catalyzed transformation of *erythro*-DGPD, as shown by DFT calculations, are remarkably similar, despite the latter being associated with a highly energetic C–C bond fragmentation reaction. This relatively low free energy barrier provides insight into how the abiotic formaldehyde elimination route under a highly alkaline condition is favored over an addition route (26). Further experiments will fully substantiate the current proposed mechanism. Specifically, single-turnover transient-state kinetic studies could help establish the true nature of the rate-limiting step, identify the putative quinone methide intermediate by its spectral properties, and discern the order of the product release.

Product inhibition of LdpA by lignostilbene may be an in vitro artifact that is not relevant in vivo as both *N. aromaticivorans* and SYK-6 encode multiple copies of *lsd*, many possessing cross-reactivities to different 4-hydroxystilbenes (19, 20, 30–33). The observed competitive product inhibition can readily be rationalized by the DFT calculation where the energy level associated with the *erythro*-DGPD and lignostilbene binding is comparable

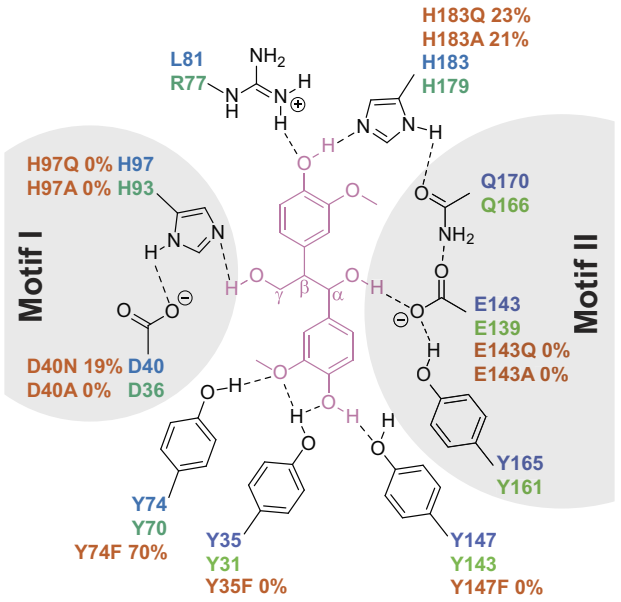

Fig. 5. Summary of LdpA mutational analysis. A diagram of the *erythro*-DGPD-bound LdpA complex. The amino acid residues are in *black* and *erythro*-DGPD is in *pink*. The residues numbering from *Na*LdpA and *Sp*LdpA are labeled in *blue* and *green*, respectively. The dashed lines represent polar interactions ≤3 Å. The activity of the *Na*LdpA variants presented is normalized to the activity of the WT enzyme and labeled in *orange*. The two catalytic motifs are noted by shaded regions. Numerical data are provided in the *SI Appendix,* Table S7.

(Fig. 6*B*). Additionally, there might be a second nonproductive stilbene binding site as indicated by the *Na*LdpA·resveratrol complex structure (*SI Appendix,* Fig. S10). The second site overlaps significantly with the first productive DGPD binding site and thus would still elicit competitive inhibition. Regardless, the inhibition is likely to be mitigated in vivo as lignostilbene is quickly consumed by the LSD to form vanillin. Multiple LSD homologs for both SYK-6 and *N. aromaticivorans* likely evolved to ensure the forward flux of the metabolite, thereby preventing product inhibition. However, a specific LSD may be more strongly tied to a dimer-specific catabolism through some form of regulation, as shown in the catabolism of DCA (19). Moreover, it is not known whether the *erythro*-DGPD γ-formaldehyde lyase from TMY1009 is homologous to the LdpA described in this study. Indeed, both enzymes are functionally analogous, catalyzing a cofactorless nonoxidative deformylation of *erythro*-DGPD to produce lignostilbene and function maximally within the same pH range (17). However, their molecular weight and quaternary structures appear to be different: namely a dimer for the TMY1009 lyase and a trimer for LdpA. These observations may suggest yet another enzyme system for the deformylation of *erythro*-DGPD.

Comparison between the reactions catalyzed by LdpA to other enzymatic systems suggests an evolutionary and chemically divergent nonoxidative alcohol decarboxylation paradigm. Primary alcohols are typically oxidized to either an aldehyde or a carboxylate prior to its removal. For example, the catabolism of DCA requires the successive oxidation of the nonphenolic alcohols to carboxylates (34). The central furan carboxylate of 5-(2-carboxyvinyl)-2-(4-hydroxy-3-methoxyphenyl)-7-methoxy-2,3-dihydrobenzofuran-3-carboxylic acid (DCA-CC) is then removed by the stereospecific DUF3237 decarboxylases (PhcF and PhcG) to produce 3-[4-hydroxy-3-(4-hydroxy-3-methoxystyryl)-5-methoxyphenyl] acrylic acid (DCA-S), a stilbene (34–36). An alternative paradigm for nonoxidative C–C bond fragmentation producing formaldehyde as a product can be found in aldolases – these enzymes catalyze reversible addition between a carbonyl and an alcohol to produce a

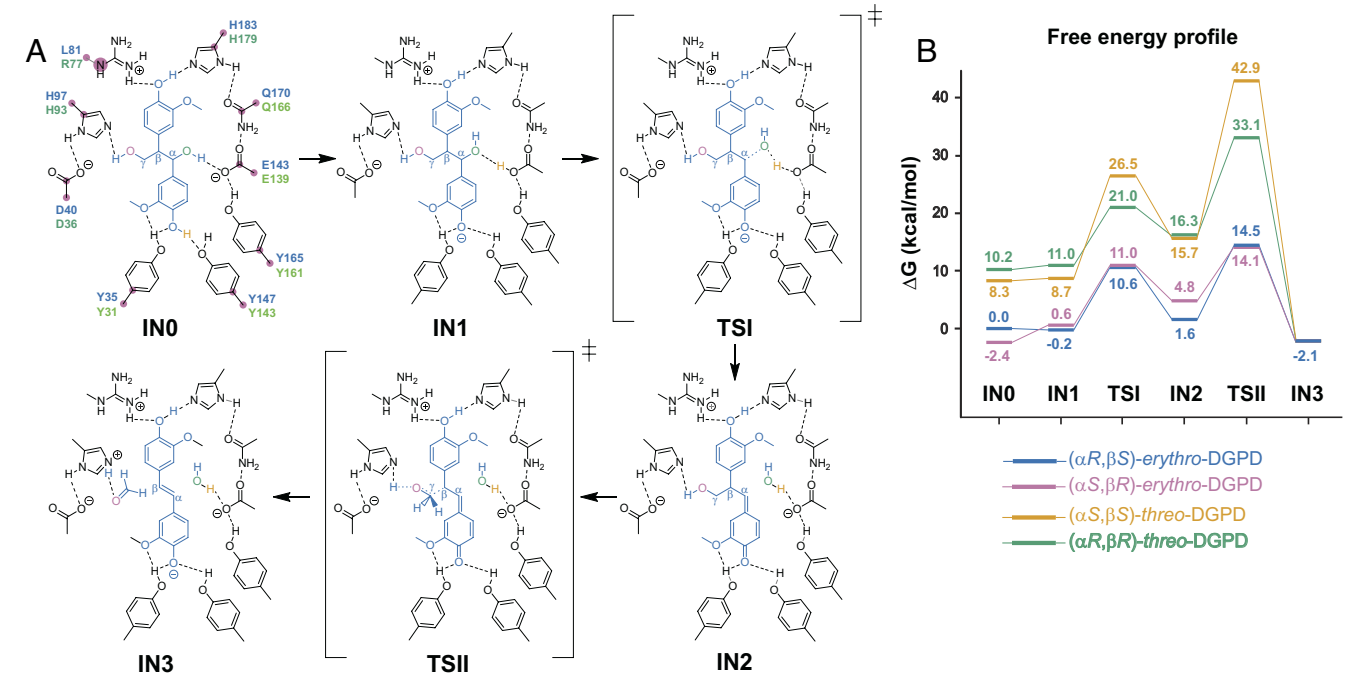

Fig. 6. Molecular mechanism of LdpA. (*A*) Proposed catalytic mechanism of LdpA. The amino acid side chain numberings for *Na*LdpA and *Sp*LdpA are highlighted in *blue* and *green*, respectively. The atoms highlighted in *pink* are frozen in the DFT computations and are only shown for the IN0. The oxygen atoms for the C_α and C_γ-hydroxyl groups are in *green* and *pink*, respectively. The C_α -phenolic proton is in *orange*. The partial bonds in transition states are denoted in dotted line. (*B*) Free energy profiles associated with the different intermediates and transition states associated with the different enantiomeric form of DGPD. All energies are in kcal/mol. DFT methods: B3LYP-D3(BJ)/6-31G(d,p), SCRF = (CPCM, Solvent = water), with Grimme correction for entropy and Head–Gordon correction for enthalpy. The numerical data are provided in the *SI Appendix,* Table S9.

β-hydroxy carbonyl. For example, 3-hexulose-6-phosphate synthetase catalyzes the reversible aldol reaction between formaldehyde and D-5-ribulose 5-phosphate, which may work in tandem with 6-phospho-3-hexuloisomerase to shift the reaction equilibrium (37, 38). While most bacterial aldolases are divalent metal dependent, eukaryotic aldolases represent a cofactorless system that utilizes a catalytic lysine to form a covalent Schiff-base conjugate (39). Nonetheless, the catalytic principles and enzyme architecture of examples described differ from those of LdpA.

Both enantiomers of *erythro*-DGPD have been previously isolated from plant materials and primarily studied for their therapeutic use as antioxidants (40–42). This suggests the prevalence of the β-1 linkages in nature and their presence is not solely from the inadvertent transformation during biomass processing or lignin extraction (43). Indeed, β-1 linkages have also been reported from prior NMR measurements of milled wood lignin, constituting from less than 3% or up to 10%, depending on the plant origin (44–48). Several variants of the β-1 dimer have been reported in the literature with different extents of aromatic methoxylation, likely stemming from their monolignol precursors (41). Other derivatives of *erythro*-DGPD contain modifications at the C_α position including C_α-carbonyl, C_α-methoxy, and C_α-*O*-glucoside, suggesting an added diversity within β-1 dimers (41, 42).

The diastereomer specificity displayed by LdpA contrasts with the enantioselectivity of the enzymes involved in the catabolism of β-*O*-4 and β-5 dimers (34, 49–51). Unfortunately, none of the LdpA homologs tested in this study affected the *threo*-DGPD. Currently, the catabolic pathway for *threo*-DGPD has not been reported to our knowledge and its conversion may require cometabolism of related aromatics, as SYK-6 cannot grow on *threo*-DGPD as a sole carbon and energy source (*SI Appendix,* Fig. S23). The characterization of this hitherto unknown pathway would be imperative for more complete lignin valorization, especially as both diastereomers of β-1 exist in nature, often at near-equal proportions (52).

Overall, the identification of LdpA associates the NTF-2-like enzyme family with the transformation of lignin-derived aromatic dimers, thus expanding the catabolic repertoire for engineering microbial biocatalysts with wider catabolic capabilities for biological funneling of lignin (5). Additionally, the characterization of LdpA activity expands the range of reactions catalyzed by the NTF-2-like protein family to include a formaldehyde-eliminating lyase reaction.

Materials and Methods

Chemicals. Commercially procured chemical and reagents were of analytical grade and used without further purification. DGPD and GPD were synthesized as described in *SI Appendix*. Lignostilbene was a kind gift from Prof. Lindsay D. Eltis.

Bacterial Strains and Growth Conditions. Bacterial strains used in this study are listed in the *SI Appendix* and grown in lysogeny broth (LB) or Wx media as described in *SI Appendix*.

DNA Manipulation and Strain Engineering. DNA was purified, manipulated, and propagated following standard protocols. The gene deletion mutant in SYK-6 was generated by allelic exchange as described in the *SI Appendix*.

Substrate Depletion. Depletion and transformation of DGPD by cell extracts were analyzed by HPLC as described in the *SI Appendix*.

Protein Production and Purification. *Na*LdpA, *Sp*LdpA, and NOV2 were produced heterologously as polyHis-tagged protein fusions and purified using chromatography as described in the *SI Appendix*. Purified proteins were flash-frozen in liquid N_2 bath and stored at −80 °C until further use.

Characterization of LdpA-Catalyzed Reaction and Kinetics. The product from the LdpA-catalyzed reaction was analyzed using HPLC. Formaldehyde was detected by using a dehydrogenase and a chromogenic assay. Kinetic parameters for *Na*LdpA and *Sp*LdpA were determined spectrophotometrically and by oxygraphy by coupling the reaction using NOV2. Detailed protocols are provided in the *SI Appendix*.

Protein Structure Determination and Biophysical Characterizations. The atomic structures, the oligomeric state in solution, the apparent melting temperature, and thermodynamic of the reaction were determined using X-ray crystallography, HPLC-SAXS, DSC, and ITC, respectively, with detailed protocols provided in *SI Appendix*.

DFT. Calculations are performed using the Gaussian 16 package (53) and described in the *SI Appendix*.

Data, Materials, and Software Availability. All relevant data are provided in the manuscript or in the *SI Appendix*. The atomic coordinates and structure factors have been deposited in the Protein Data Bank (PDB ID codes: 8ABT, 8ABU, 8ABV, and 8ABW).

ACKNOWLEDGMENTS. This work was authored in part by the National Renewable Energy Laboratory, operated by Alliance for Sustainable Energy, LLC, for the U.S. Department of Energy (DOE) under contract no. DE-AC36-08GO28308. E.K., D.J.H., M.O.K., J.E.M., A.R.P., J.K.M., and G.T.B. acknowledge funding from the Center for Bioenergy Innovation, a U.S. Department of Energy Research Center supported by the Office of Biological and Environmental Research in the DOE Office of Science. Funding for analytical chemistry and organic synthesis was provided to S.J.H., R.K., and G.T.B. by the U.S. Department of Energy Office of Energy Efficiency and Renewable Energy Bioenergy Technologies Office. The views expressed in the article do not necessarily represent the views of the DOE or the U.S. government. The U.S. government retains and the publisher, by accepting the article for publication, acknowledges that the U.S. government retains a nonexclusive, paid-up, irrevocable, worldwide license to publish or reproduce the published form of this work, or allow others to do so, for U.S. government purposes. M.Z., A.R.P., and J.E.M. acknowledge Research England for Expanding Excellence in England (E3) funding. Funding to X.C. and K.N.H. was provided by the NSF (CHE-1764328). E.M. acknowledges funding from the Noda Institute for Scientific Research, Japan. This material is based upon work supported by the U.S. Department of Energy, Office of Science, Office of Biological and Environmental Research, through an Early Career Award to J.K.M. (ERKP971). Erika Erickson is thanked for the construction of pEE001 and pEE002. Nina X. Gu, Lindsay D. Eltis, and Jennifer L. DuBois are thanked for helpful discussions. We thank the Diamond Light Source (Didcot, UK) for beamtime (proposal MX-23269), the beamline staff at I23 and I03 for support, and Nikul Khunti and Diamond B21 for their help with collecting the SAXS data. Computations were performed on the Hoffman2 cluster at UCLA and the Extreme Science and Engineering Discovery Environment (XSEDE), which is supported by the NSF (OCI-1053575). We are grateful for financial support of the National Institute of General Medical Sciences, NIH, GM124480. Tracy Hartlage and Dr. William L. Watts, Jr from Chiral Technologies Inc. are thanked for their assistance for selection, optimization, and method development for chiral chromatography.

Author affiliations: [a]Renewable Resources and Enabling Sciences Center, National Renewable Energy Laboratory, Golden, CO 80401; [b]Centre for Enzyme Innovation, School of Biological Sciences, Institute of Biological and Biomedical Sciences, University of Portsmouth, Portsmouth PO12DT, UK; [c]Department of Chemistry and Biochemistry, University of California Los Angeles, CA 90095; [d]Department of Materials Science and Bioengineering, Nagaoka University of Technology, Nagaoka, Niigata 940-2188, Japan; [e]Diamond Light Source, Harwell Science and Innovation Campus, Didcot OX11 0DE, UK; and [f]Biosciences Division, Oak Ridge National Laboratory, Oak Ridge, TN 37830

Author contributions: E.K., J.K.M., N.K., E.M., K.N.H., J.E.M., and G.T.B. designed research; E.K., M.Z., X.C., R.Kato, D.J.H., R.Katahira, S.J.H., K.J.R., and A.R.P. performed research; M.O.K., R.K., C.O., A.W., S.J.H., K.J.R., and A.R.P. contributed new reagents/analytic tools; E.K., M.Z., X.C., R.K., Y.Z., A.R.P., N.K., E.M., K.N.H., J.E.M., and G.T.B. analyzed data; and E.K., M.Z., X.C., J.E.M., and G.T.B. wrote the paper.

1. A. J. Ragauskas *et al.*, Lignin valorization: Improving lignin processing in the biorefinery. *Science* **344**, 1246843 (2014).
2. G. T. Beckham, C. W. Johnson, E. M. Karp, D. Salvachua, D. R. Vardon, Opportunities and challenges in biological lignin valorization. *Curr. Opin. Biotechnol.* **42**, 40–53 (2016).
3. J. G. Linger *et al.*, Lignin valorization through integrated biological funneling and chemical catalysis. *Proc. Natl. Acad. Sci. U.S.A.* **111**, 12013–12018 (2014).
4. O. Y. Abdelaziz *et al.*, Biological valorization of low molecular weight lignin. *Biotechnol. Adv.* **34**, 1318–1346 (2016).
5. N. Kamimura *et al.*, Bacterial catabolism of lignin-derived aromatics: New findings in a recent decade: Update on bacterial lignin catabolism. *Environ. Microbiol. Rep.* **9**, 679–705 (2017).
6. C. W. Johnson *et al.*, Innovative chemicals and materials from bacterial aromatic catabolic pathways. *Joule* **3**, 1523–1537 (2019).
7. J. Becker, C. Wittmann, A field of dreams: Lignin valorization into chemicals, materials, fuels, and health-care products. *Biotechnol. Adv.* **37**, 107360 (2019).
8. W. Schutyser *et al.*, Chemicals from lignin: An interplay of lignocellulose fractionation, depolymerisation, and upgrading. *Chem. Soc. Rev.* **47**, 852–908 (2018).
9. F. Weiland, M. Kohlstedt, C. Wittmann, Guiding stars to the field of dreams: Metabolically engineered pathways and microbial platforms for a sustainable lignin-based industry. *Metab. Eng.* **71**, 13–41 (2022).
10. T. D. Bugg, R. Rahmanpour, Enzymatic conversion of lignin into renewable chemicals. *Curr. Opin. Chem. Biol.* **29**, 10–17 (2015).
11. L. D. Eltis, R. Singh, "Chapter 11 Biological funneling as a means of transforming lignin-derived aromatic compounds into value-added chemicals" in *Lignin Valorization: Emerging Approaches* (The Royal Society of Chemistry, 2018), pp. 290–313.
12. W. S. Kontur *et al.*, *Novosphingobium aromaticivorans* uses a Nu-class glutathione *S*-transferase as a glutathione lyase in breaking the β-aryl ether bond of lignin. *J. Biol. Chem.* **293**, 4955–4968 (2018).
13. J. M. Perez *et al.*, Funneling aromatic products of chemically depolymerized lignin into 2-pyrone-4-6-dicarboxylic acid with *Novosphingobium aromaticivorans*. *Green Chem.* **21**, 1340–1350 (2019).
14. N. Kamimura, S. Sakamoto, N. Mitsuda, E. Masai, S. Kajita, Advances in microbial lignin degradation and its applications. *Curr. Opin. Biotechnol.* **56**, 179–186 (2019).
15. W. S. Kontur *et al.*, A heterodimeric glutathione *S*-transferase that stereospecifically breaks lignin's β(*R*)-aryl ether bond reveals the diversity of bacterial β-etherases. *J. Biol. Chem.* **294**, 1877–1890 (2019).
16. T. D. Bugg, M. Ahmad, E. M. Hardiman, R. Rahmanpour, Pathways for degradation of lignin in bacteria and fungi. *Nat. Prod. Rep.* **28**, 1883–1896 (2011).
17. K. Kishi, N. Habu, M. Samejima, T. Yoshimoto, Purification and some properties of the enzyme catalyzing the Cγ-elimination of a diarylpropane-type lignin model from *Pseudomonas paucimobilis* TMY1009. *Agric. Biol. Chem.* **55**, 1319–1323 (1991).
18. G. N. Presley *et al.*, Pathway discovery and engineering for cleavage of a β-1 lignin-derived biaryl compound. *Metab. Eng.* **65**, 1–10 (2021).
19. N. Kamimura *et al.*, LsdD has a critical role in the dehydrodiconiferyl alcohol catabolism among eight lignostilbene α,β-dioxygenase isozymes in *Sphingobium* sp. strain SYK-6. *Int. Biodeterior. Biodegrad.* **159**, 105208 (2021).
20. E. Kuatsjah *et al.*, Structural and functional analysis of lignostilbene dioxygenases from *Sphingobium* sp. SYK-6. *J. Biol. Chem.* **296**, 100758 (2021).
21. T. L. Bullock, W. D. Clarkson, H. M. Kent, M. Stewart, The 1.6 Å resolution crystal structure of nuclear transport factor 2 (NTF2). *J. Mol. Biol.* **260**, 422–431 (1996).
22. S. Bhowmik *et al.*, Structure and functional characterization of a bile acid 7α dehydratase BaiE in secondary bile acid synthesis. *Proteins* **84**, 316–331 (2016).
23. T. Lundqvist *et al.*, Crystal structure of scytalone dehydratase - a disease determinant of the rice pathogen, *Magnaporthe grisea*. *Structure* **2**, 937–944 (1994).
24. M. Okai *et al.*, Crystal structure of γ-hexachlorocyclohexane dehydrochlorinase LinA from *Sphingobium japonicum* UT26. *J. Mol. Biol.* **403**, 260–269 (2010).
25. M. Zeug *et al.*, Crystal structures of non-oxidative decarboxylases reveal a new mechanism of action with a catalytic dyad and structural twists. *Sci. Rep.* **11**, 3056 (2021).
26. J. Ralph, R. M. Ede, N. P. Robinson, L. Main, Reactions of ß-aryl lignin model quinone methides with anthrahydroquinone and anthranol. *J. Wood Chem. Technol.* **7**, 133–160 (1987).
27. A. Wagner, R. Duman, K. Henderson, V. Mykhaylyk, In-vacuum long-wavelength macromolecular crystallography. *Acta Crystallogr. D Struct. Biol.* **72**, 430–439 (2016).
28. L. Holm, DALI and the persistence of protein shape. *Protein Sci.* **29**, 128–140 (2020).
29. L. Trantirek *et al.*, Reaction mechanism and stereochemistry of γ-hexachlorocyclohexane dehydrochlorinase LinA. *J. Biol. Chem.* **276**, 7734–7740 (2001).
30. E. K. Marasco, C. Schmidt-Dannert, Identification of bacterial carotenoid cleavage dioxygenase homologues that cleave the interphenyl α,β double bond of stilbene derivatives via a monooxygenase reaction. *ChemBioChem* **9**, 1450–1461 (2008).
31. E. Kuatsjah *et al.*, Identification of functionally important residues and structural features in a bacterial lignostilbene dioxygenase. *J. Biol. Chem.* **294**, 12911–12920 (2019).
32. R. P. McAndrew *et al.*, Structure and mechanism of NOV1, a resveratrol-cleaving dioxygenase. *Proc. Natl. Acad. Sci. U.S.A.* **113**, 14324–14329 (2016).
33. X. Sui *et al.*, Structure and spectroscopy of alkene-cleaving dioxygenases containing an atypically coordinated non-heme iron center. *Biochemistry* **56**, 2836–2852 (2017).
34. K. Takahashi, K. Miyake, S. Hishiyama, N. Kamimura, E. Masai, Two novel decarboxylase genes play a key role in the stereospecific catabolism of dehydrodiconiferyl alcohol in *Sphingobium* sp. strain SYK-6. *Environ. Microbiol.* **20**, 1739–1750 (2018).
35. U. K. Bagha, J. K. Satpathy, G. Mukherjee, C. V. Sastri, S. P. de Visser, A comprehensive insight into aldehyde deformylation: Mechanistic implications from biology and chemistry. *Org. Biomol. Chem.* **19**, 1879–1899 (2021).
36. E. N. Marsh, M. W. Waugh, Aldehyde decarbonylases: Enigmatic enzymes of hydrocarbon biosynthesis. *ACS Catal.* **3** (2013), 10.1021/cs400637t.
37. N. Kato, N. Miyamoto, M. Shimao, C. Sakazawa, 3-hexulose phosphate synthase from a new facultative methylotroph, *Mycobacterium gastri* MB 19. *Agric. Biol. Chem.* **52**, 2659–2661 (1988).
38. S. Brott *et al.*, Connecting algal polysaccharide degradation to formaldehyde detoxification. *ChemBioChem* **23**, e202200269 (2022).
39. K. Tittmann, Sweet siblings with different faces: The mechanisms of FBP and F6P aldolase, transaldolase, transketolase and phosphoketolase revisited in light of recent structural data. *Bioorg. Chem.* **57**, 263–280 (2014).
40. S. Mitsuhashi, T. Kishimoto, Y. Uraki, T. Okamoto, M. Ubukata, Low molecular weight lignin suppresses activation of NF-kappaB and HIV-1 promoter. *Bioorg. Med. Chem.* **16**, 2645–2650 (2008).
41. L. Zhou *et al.*, Neuroprotective effects of 1,2-diarylpropane type phenylpropanoid enantiomers from red raspberry against H_2O_2-induced oxidative stress in human neuroblastoma SH-SY5Y cells. *J. Agric. Food Chem.* **66**, 331–338 (2018).
42. K. Yoshikawa, N. Mimura, S. Arihara, Isolation and absolute structures of enantiomeric 1,2-bis(4-hydroxy-3-methoxyphenyl)-1,3-propanediol 1-*O*-glucosides from the bark of *Hovenia trichocarpa*. *J. Nat. Prod.* **61**, 1137–1139 (1998).
43. G. Gellerstedt, L. Zhang, Reactive lignin structures in high yield pulping: Part 1. Structures of the 1,2-diarylpropane-1,3-diol type. *Nord. Pulp Paper Res. J.* **6**, 136–139 (1991).
44. R. M. Ede, J. Ralph, K. M. Torr, B. S. W. Dawson, A 2D NMR investigation of the heterogeneity of distribution of diarylpropane structures in extracted *Pinus radiata* lignins. *Holzforschung* **50**, 161–164 (1996).
45. R. M. Ede, J. Ralph, Assignment of 2D TOCSY spectra of lignins: The role of lignin model compounds. *Magn. Reson. Chem.* **34**, 261–268 (1996).
46. C. Lapierre, B. Pollet, B. Monties, Heterogeneous distribution of diarylpropane structures in spruce lignins. *Phytochem.* **30**, 659–662 (1991).
47. R. M. Ede, G. Brunow, L. K. Simola, J. Lemmetyinen, Two-dimensional ^1H–^1H chemical shift correlation and J-resolved NMR studies on isolated and synthetic lignins. *Holzforschung* **44**, 95–101 (1990).
48. T. Higuchi, Lignin biochemistry: Biosynthesis and biodegradation. *Wood Sci. Technol.* **24**, 23–63 (1990).
49. Y. Sato *et al.*, Identification of three alcohol dehydrogenase genes involved in the stereospecific catabolism of arylglycerol-β-aryl ether by *Sphingobium* sp. strain SYK-6. *Appl. Environ. Microbiol.* **75**, 5195–5201 (2009).
50. E. Masai *et al.*, Roles of the enantioselective glutathione *S*-transferases in cleavage of β-aryl ether. *J. Bacteriol.* **185**, 1768–1775 (2003).
51. K. Takahashi *et al.*, Membrane-associated glucose-methanol-choline oxidoreductase family enzymes PhcC and PhcD are essential for enantioselective catabolism of dehydrodiconiferyl alcohol. *Appl. Environ. Microbiol.* **81**, 8022–8036 (2015).
52. K. Lundquist, S. Li, "Structural analysis of lignin and lignin degradation products" in *10th International Symposium on Wood and Pulping Chemistry, Main Symposium, Yokohama, Japan, June 7–10, 1999* Chalmers University of Technology (1999), p. 2.
53. M. J. Frisch, Gaussian 16 Rev. C.01. Gaussian Inc. Wallingford, CT (2016).